

# Predominance of the Kitaev interaction in a three-dimensional honeycomb iridate: from *ab-initio* to spin model

Heung-Sik Kim,<sup>1</sup> Eric Kin-Ho Lee,<sup>1</sup> and Yong Baek Kim<sup>1,2</sup>

<sup>1</sup>*Department of Physics and Center for Quantum Materials, University of Toronto, 60 St. George St., Toronto, Ontario, M5S 1A7, Canada*

<sup>2</sup>*Canadian Institute for Advanced Research / Quantum Materials Program, Toronto, Ontario MSG 1Z8, Canada*

The recently discovered three-dimensional hyperhoneycomb iridate,  $\beta$ -Li<sub>2</sub>IrO<sub>3</sub>, has raised hopes for the realization of dominant Kitaev interaction between spin-orbit entangled local moments due to its near-ideal lattice structure. If true, this material may lie close to the sought-after quantum spin liquid phase in three dimensions. Utilizing *ab-initio* electronic structure calculations, we first show that the spin-orbit entangled basis,  $j_{\text{eff}} = 1/2$ , correctly captures the low energy electronic structure. The effective spin model derived in the strong coupling limit supplemented by the *ab-initio* results is shown to be dominated by the Kitaev interaction. We demonstrated that the possible range of parameters is consistent with a non-coplanar spiral magnetic order found in a recent experiment. All of these analyses suggest that  $\beta$ -Li<sub>2</sub>IrO<sub>3</sub> may be the closest among known materials to the Kitaev spin liquid regime.

*Introduction* – Kitaev’s exact solution of a quantum spin-liquid on a spin-1/2 honeycomb model has spurred considerable interest in the search for a material realization[1, 2]. Of particular focus is the family of quasi-two-dimensional (2D) honeycomb iridate materials  $\alpha$ -A<sub>2</sub>IrO<sub>3</sub> ( $A = \text{Na, Li}$ , hereafter  $\alpha$ AIO), where iridium (Ir) ions form decoupled layers of honeycomb lattices[3, 4] and have been argued to host spin-orbital entangled  $j_{\text{eff}} = 1/2$  degrees of freedom[5–7]. Due to the interplay of strong atomic spin-orbit coupling (SOC) and correlation effects, these  $j_{\text{eff}} = 1/2$  moments in the ideal  $\alpha$ AIO structure interact in the highly anisotropic manner described by the Kitaev model[8]. In addition to these Kitaev-type exchanges, the symmetries of the ideal structure also permit additional exchanges that generate a plethora of interesting phases of matter[9]. In reality, however, these materials possess sizeable monoclinic distortions that deform the octahedral oxygen cages surrounding Ir ions[4, 10]. These distortions lower the symmetry of the system and therefore complicate the description of these materials. Thus far, a consensus on the minimal model required to describe this family of 2D honeycomb iridates has yet been reached; a distortion-free analog of these honeycomb iridates may offer a more direct path towards the realization of Kitaev physics.

The timely discovery and synthesis[12, 13] of the hyperhoneycomb  $\beta$ -Li<sub>2</sub>IrO<sub>3</sub> (hereafter  $\beta$ LIO) may present such an exciting opportunity. Much like its 2D counterpart, the Kitaev model on the ideal, 3D hyperhoneycomb lattice supports an exact spin liquid ground state[14–17]. In addition, the distortion-free, classical pseudospin-1/2 model on the hyperhoneycomb lattice also supports a myriad of complex magnetic phases[11]. Moreover, interesting topological phases have been predicted on this lattice[18]. These previous results illustrate the possibilities that may be realizable in  $\beta$ LIO; however, they rely on the use of the  $j_{\text{eff}} = 1/2$  degrees of freedom in the low-energy description of  $\beta$ LIO, which has not been justified microscopically. Furthermore, whether the near-ideal structure of  $\beta$ LIO can give rise to a simple minimal pseudospin model dominated by the Kitaev exchange has so far not been validated. Also, with the recent experimental

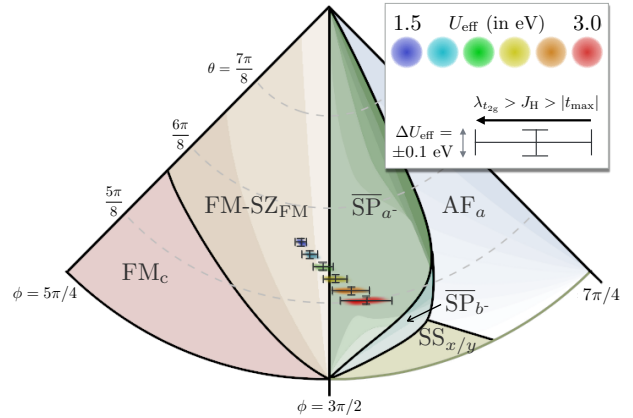


FIG. 1. (Color online) Phase diagram of the  $J$ - $K$ - $\Gamma$  model reproduced from Ref. [11], overlaid with density distributions of exchange interaction parameters estimated from *ab-initio* results for  $\beta$ LIO; see main text for details. Six shaded areas with different colors represent relevant  $U_{\text{eff}}$  values ranging from 1.5 to 3.0 eV in increments of 0.3 eV. Vertical and horizontal markers on the shaded areas depict the variation of  $U_{\text{eff}}$  and  $J_H$ , respectively, as shown in the inset. Note that, when  $U_{\text{eff}} \geq 2.4$  eV, corresponding phases lie within the green  $\overline{\text{SP}}_{\alpha^-}$  spiral phase area.  $\overline{\text{SP}}_{\alpha^-}$  phase is consistent with the magnetic order observed in the experimental work of Ref. [12]. For detailed discussion of the other phases, see Ref. [11].

observation of a magnetic spiral order in  $\beta$ LIO, any minimal model and its accompanying parameters must also be capable of predicting the observed order: this provides a stringent test of feasibility for any model describing  $\beta$ LIO.

In this letter, we tackle these issues by combining results of our *ab-initio* electronic structure calculations and a strong-coupling theory to arrive at a  $j_{\text{eff}} = 1/2$  model to describe  $\beta$ LIO. From our *ab-initio* band structure results, we find that the low-energy states can be described in terms of localized  $j_{\text{eff}} = 1/2$  states because of the large atomic SOC present in Ir. In fact, the magnitude of SOC in the paramagnetic state is enhanced by the electron interactions in Ir  $d$  orbitals, which is consistent with recent observations in several  $4d$  and  $5d$  transi-

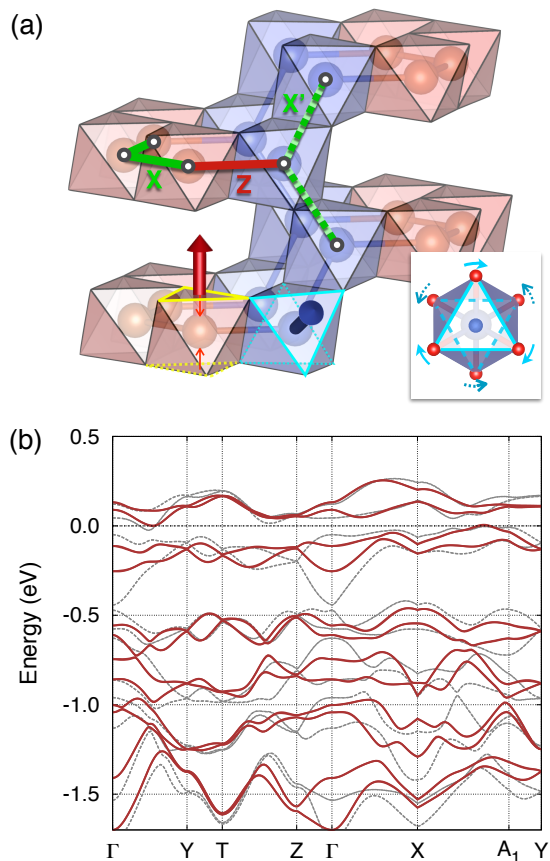


FIG. 2. (Color online) (a) Network of  $\text{IrO}_6$  octahedra in the hyperhoneycomb lattice. The two distinct nearest-neighbor (NN) bonds, X and Z, are depicted as solid green and red lines, respectively. X and X' bonds are symmetry equivalent, whereas Z bonds are distinct. Emerging from the octahedra, the red and blue arrows point in the direction of the trigonal distortions for red and blue  $\text{IrO}_6$  octahedra respectively. The trigonal distortion, which consists of the compression and rotations of the opposing oxygen triangles, is illustrated in the figure and in the inset. (b) shows the band structure with the presence of spin-orbit coupling (SOC). Solid red and dashed grey curves are the band structure of the experimental and ideal structures, respectively.

tion metal compounds[19–21]. To go beyond the limitation of *ab-initio* calculations in treating electron interactions, we employ the strong-coupling expansion recently proposed in [9] to arrive at a minimal pseudospin-1/2 model. Due to the near-ideal structure of  $\beta\text{LIO}$ , we discover that the resulting pseudospin model is near-isotropic while both distortion-induced and further neighbor interactions are small. Remarkably, the estimated exchange interactions places the model near the ferromagnetic Kitaev limit and within a region where the classical ground state agrees well with the experimentally-observed spiral phase[12]. Our results are summarized in Fig. 1 and elaborated in the rest of this work.

*Structure and ab-initio calculations* –  $\beta\text{LIO}$  is a member of the generic three-dimensional (3D) harmonic honeycomb iridate series[22], which are structural variants of 2D-

honeycomb iridates  $\alpha\text{AIO}$ . The hyperhoneycomb lattice is composed of a tri-coordinated network of edge-shared  $\text{IrO}_6$  octahedra as shown in Fig. 2(a). There are two types of nearest-neighbor (NN) bonds in this network: we denote these bonds as X and Z. Despite being symmetry-inequivalent, these two bonds are almost identical owing to their similar local crystal structures as revealed by recent structural analysis[12, 13].

The crystal structure refinement also revealed nearly ideal  $\text{IrO}_6$  octahedra compared to those from  $\alpha\text{LIO}$ : standard deviations of the Ir-O bond length and O-Ir-O bond angles in  $\beta\text{LIO}$  (0.002 Å and  $2.77^\circ$ ) are much smaller than those in  $\alpha\text{LIO}$  (0.050 Å and  $4.56^\circ$ )[10]. Since finite standard deviations in O-Ir-O bond angles is a result of trigonal distortion in the  $\text{IrO}_6$  octahedra, the small value present in  $\beta\text{LIO}$  indicates that trigonal distortions are indeed small in this compound (the directions of trigonal distortion are shown as colored arrows in the figure). The nearly ideal  $\text{IrO}_6$  octahedra in  $\beta\text{LIO}$  suggest that local crystal fields are principally cubic in symmetry, therefore the spin-orbital entangled  $j_{\text{eff}} = 1/2$  states would be a good basis to construct a low-energy description of this material in the presence of strong SOC.

To validate the use of  $j_{\text{eff}} = 1/2$  states in the low-energy description of  $\beta\text{LIO}$ , we turn to *ab-initio* electronic structure calculations[23]. The band dispersions of the ideal and experimental structures with SOC can be seen in Fig. 2(b). The dispersions from the experimental structure (solid red curves) and those from ideal one (dashed grey curves) share similar overall shape, especially near the chemical potential. The separation between the upper eight bands and the lower sixteen bands (including Kramers degeneracies) can be clearly seen in the figure, suggesting the formation of  $j_{\text{eff}} = 1/2$  and  $j_{\text{eff}} = 3/2$  bands[24].

In Fig. 3(a), we show the  $j_{\text{eff}}$ -projected band dispersions and density of state (PDOS) in the presence of SOC based on the experimental structure. The Projection is done by taking inner products between the atomic  $j_{\text{eff}}$  states and the Bloch state represented in terms of the local pseudo-atomic orbital basis. Weights of the  $j_{\text{eff}}=1/2$  and  $3/2$  components within each Bloch state are depicted as the size of red and blue circles, respectively, in the band plots. The large  $j_{\text{eff}} = 1/2$  PDOS weight in the upper eight bands—the closest bands to the Fermi level—indicates the development of  $j_{\text{eff}} = 1/2$  bands and confirms that the basis states relevant to the low-energy description of  $\beta\text{LIO}$  possess mostly  $j_{\text{eff}} = 1/2$  character. The effect of electron correlations inherent to Ir  $t_{2g}$  orbital further enhances the  $j_{\text{eff}} = 1/2$  character as shown in Fig. 3(b), where effective on-site Coulomb interaction  $U_{\text{eff}} \equiv U - J_H$  is included within the DFT+ $U$  formalism ( $J_H$  is Hund's coupling; for details see Sec. A in Supplementary Materials).[25] As  $U_{\text{eff}} = 3.0$  eV is added, the separation between the  $j_{\text{eff}} = 1/2$  and  $j_{\text{eff}} = 3/2$  states becomes enlarged. This SOC enhancement is also manifested in the increased magnitude of the effective  $t_{2g}$  SOC  $\lambda_{t_{2g}}$  as shown in Table I, which is obtained from the on-site matrix elements in the Wannier orbital calculations [26]. Such behavior has also been reported in other 4d

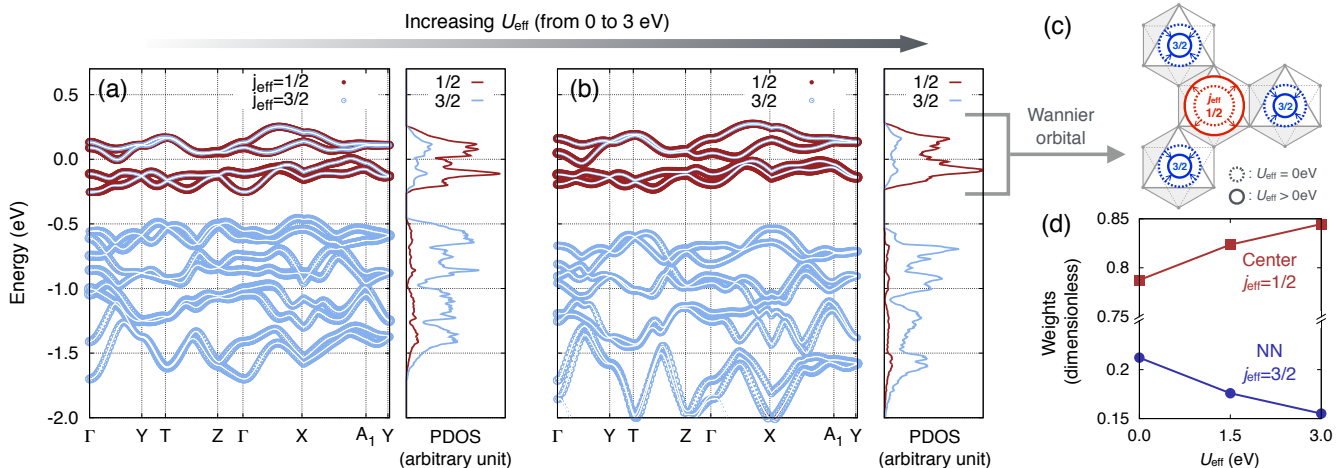


FIG. 3. (Color online) (a,b) Band structure and density of states (DOS) projected onto the  $j_{\text{eff}}$  states in the presence of SOC (a) without and (b) with the on-site Coulomb interaction  $U_{\text{eff}} = 3.0$  eV. (c) shows the schematic shape of the  $j_{\text{eff}}=1/2$ -like Wannier orbital constructed from the  $j_{\text{eff}}=1/2$ -dominated bands near the Fermi level. Dashed and solid circles depict the Wannier orbitals from calculations without and with finite  $U_{\text{eff}}$ , respectively. Weights of the central  $j_{\text{eff}}=1/2$  and nearest-neighboring  $j_{\text{eff}}=3/2$  tail in the orbital are shown in (d) as a function of  $U_{\text{eff}}$ .

$U_{\text{eff}}$ (eV)	0.0	1.5	3.0
$\lambda_{t_{2g}}$	0.401	0.482	0.516
$t_1$			
Z	+0.085	+0.077	+0.064
X	+0.083	+0.074	+0.058
$ t_2 $			
Z	0.238	0.255	0.270
X	0.260	0.276	0.289
$t_3$			
Z	-0.162	-0.119	-0.060
X	-0.153	-0.110	-0.055

TABLE I. Magnitude of SOC within the Ir  $t_{2g}$  states and  $t_{2g}$  hopping terms from Wannier orbital calculations in the presence of  $U_{\text{eff}}$ . We adopt the coordinate system such that  $t_2$  is negative for both Z and X bonds. By symmetry,  $t_2$  is positive for the X' bonds.

and  $5d$  orbital systems [27][19–21].

The effects caused by electron correlations in the low-energy  $j_{\text{eff}} = 1/2$ -dominated states deserve further comment. Fig. 3(c) shows the schematic shape of Wannier orbitals constructed from the  $j_{\text{eff}} = 1/2$  energy window, which can be considered as the local orbitals that span the low-energy subspace. Owing to the nearly ideal  $\text{IrO}_6$  octahedra (as supported by the small amount of trigonal distortion of less than 100 meV), the Wannier orbitals consist of pure  $j_{\text{eff}} = 1/2$  character on the center Ir site, while it has  $j_{\text{eff}} = 3/2$  tails on the NN sites. Similar features have been reported in  $\alpha\text{NIO}$  and  $\alpha\text{LIO}$ [28, 29], which mirrors the remnant molecular orbital character originating from the  $t_{2g}$  hopping[30]. As  $U_{\text{eff}}$  is included and  $\lambda_{t_{2g}}$  is enhanced, the  $j_{\text{eff}} = 1/2$  character becomes more dominant while  $j_{\text{eff}} = 3/2$  components on the NN sites decreases as shown in Fig. 3(c) and (d). The  $j_{\text{eff}} = 1/2$ -like Wannier orbital is more localized accordingly, which makes the low-energy description of  $\beta\text{LIO}$  in terms of the localized  $j_{\text{eff}} = 1/2$  states more feasible in the strong coupling limit.

$t_{2g}$  Wannier orbital hopping amplitudes – For a detailed understanding of how the near-ideal structure of  $\beta\text{LIO}$  is man-

ifested in the electronic band structure, we calculated the Ir  $t_{2g}$  hopping amplitudes from the Wannier orbitals in the experimental structure. Table I shows the magnitude of the three largest hopping terms— $t_1$ ,  $t_2$ , and  $t_3$ —as the value of  $U_{\text{eff}}$  changes ( $U_{\text{eff}} = 0.0$  eV, 1.5 eV, and 3.0 eV, and SOC is included in the calculation); see Sec. B and Fig. S1(a) in Supplementary Materials and Ref. [31] for illustration of these hopping processes. Since the Ir-Ir bond lengths and Ir-O-Ir bond angles are similar on the two inequivalent bonds of  $\beta\text{LIO}$  (X and Z bonds), the values of their respective hopping amplitudes are expected to be similar. Indeed, by comparing the hopping amplitudes between the two inequivalent NN bonds, we observe small anisotropies between the X and Z bonds ( $< 10\%$ ), which reflects the close-to-ideal structure of  $\beta\text{LIO}$ .

The evolution of the NN hopping amplitudes as we include on-site Coulomb interactions can be seen in Table I. As  $U_{\text{eff}}$  increases,  $|t_2|$  increases while  $t_1$  and  $t_3$  decrease. Such behavior is understood in terms of the enhanced hybridization between the Ir  $t_{2g}$  and oxygen  $p$  states in the presence of  $U_{\text{eff}}$ . Inclusion of  $U_{\text{eff}}$  pushes the  $j_{\text{eff}}=3/2$  states down energetically so that they become closer to the oxygen  $p$  states. This leads to increased hybridization between the Ir  $t_{2g}$  and oxygen  $p$  states, which yields the enhancement of oxygen-mediated  $t_2$  (and the reduction of  $t_1$  and  $t_3$ ).

*Strong-coupling minimal model and experimental spiral phase* – Having validated the use of the  $j_{\text{eff}} = 1/2$  basis and the similarity of hopping amplitudes between inequivalent bonds, we can now construct an effective model to describe the low-energy properties of  $\beta\text{LIO}$  in the large- $U$  limit. Following the derivation in Ref. [9], we start with localized  $j_{\text{eff}} = 1/2$  states then perform a strong-coupling expansion using NN  $t_{2g}$  hopping amplitudes[32]. In the presence of Hund's coupling  $J_H$ , we arrive at a NN,  $j_{\text{eff}} = 1/2$  model with highly

anisotropic pseudospin exchanges

$$H = \sum_{\langle ij \rangle \in \alpha(\beta\gamma)} J^\alpha S_i \cdot S_j + K^\alpha S_i^\alpha S_j^\alpha + \Gamma^\alpha (S_i^\beta S_j^\gamma + S_i^\gamma S_j^\beta),$$

where  $S_i$  is the  $j_{\text{eff}} = 1/2$  pseudospin on site  $i$ ,  $\alpha$  labels the NN  $\langle ij \rangle$  bond by its Kitaev component, and  $\beta$  and  $\gamma$  denote the two non-Kitaev components of the  $\langle ij \rangle$ -bond. The exchanges  $J$ ,  $K$ , and  $\Gamma$  are functions of the hopping amplitudes  $t_1$ - $t_3$ , strength of Hund's coupling  $J_H$ , SOC  $\lambda$ , and the on-site Coulomb interaction  $U$ : the relation between these quantities are given in Sec. D in [Supplementary Materials](#).

To establish the region in the parameter space that best models  $\beta$ LIO, the following statistical analysis was employed. First, the hopping amplitudes and SOC values in Table I were interpolated as a function of  $U_{\text{eff}}$ . Next,  $U_{\text{eff}}$  and  $J_H$  were treated as independent variables with choices of ranges  $1.5 < U_{\text{eff}} < 3.0$  eV and  $|t_2| < J_H < \lambda_{t_{2g}}$  (note that  $t_2$  is the largest hopping term)[33], due to the difficulty in determining specific values of  $U_{\text{eff}}$  and  $J_H$ . In order to present the phase evolution as a function of  $U_{\text{eff}}$ , we chose six  $U_{\text{eff}}$  intervals centered at 1.5, 1.8, 2.1, 2.4, 2.7, and 3.0 eV with ranges  $\Delta U_{\text{eff}} = \pm 0.1$  eV. From these parameters, six possible ranges of the exchange parameters were estimated as shown in the inset of Fig. 1[34]. We found that the mean anisotropies between X and Z bonds in  $J$ ,  $K$ , and  $\Gamma$  are 3%, 15%, and  $< 1\%$  respectively relative to the largest energy scale, which is the Kitaev exchange. As a first approximation, we treated all exchanges as isotropic between the X and Z bonds, which yields the NN Hamiltonian studied in the classical limit in Ref. [11]. Lastly, we overlaid the density distributions of the exchange parameters on top of the relevant portion of the classical phase diagram reproduced from Ref. [11], thereby yielding Fig. 1.

The phase diagram is the quarter of a polar plot near the ferromagnetic Kitaev limit: The angular coordinate  $\phi$  shows the ratio between  $J$  and  $K$  —  $\tan(\phi) = J/K$ . Meanwhile, the radial coordinate depicts the strength of  $\Gamma$  —  $\theta \in (\pi/2, \pi)$ ,  $\tan \theta = \sqrt{J^2 + K^2}/\Gamma$ . The bottom boundary of the half-ring ( $\theta = \pi/2$ ,  $\phi = 3\pi/2$ ) is the Heisenberg-Kitaev limit ( $\Gamma = 0$ ) and the origin ( $\theta = \pi$ ) is the pure  $\Gamma$  limit. As seen in the figure, the NN exchanges in  $\beta$ LIO are likely dominated by a large, ferromagnetic Kitaev exchange, perturbed by small  $|J|$  and  $|\Gamma|$ . Note that, higher  $U_{\text{eff}}$  and  $J_H$  prefer smaller  $\theta$  (larger  $K$ ) and smaller  $\phi$ , respectively.

We find that, when  $U_{\text{eff}} \geq 2.4$  eV, the corresponding phases lie within area of the spiral phase  $\overline{\text{SP}}_{\alpha^-}$ . Remarkably, this non-coplanar spiral magnetic phase possesses the same symmetries as the experimentally determined magnetic order.[11, 12] In other words, using the *ab-initio* hopping and SOC parameters, the resulting exchange parameters in the isotropic  $J$ - $K$ - $\Gamma$  pseudospin model results in a classical ground state that agrees with the experimental magnetic order.

*Discussion and Conclusion* – Although we have shown that the  $j_{\text{eff}} = 1/2$  states form a valid basis as a consequence of the small amount of distortions present, the difference between the dispersions of the ideal and experimental structures away

from the Fermi level are due to these distortions and the resulting bond anisotropies. However, in the context of the effective pseudospin model, we have shown that these non-idealities are negligible for the  $J$  and  $\Gamma$  exchanges. The Kitaev exchange, on the other hand, is more anisotropic between the X and Z bonds, but we speculate that the  $\overline{\text{SP}}_{\alpha^-}$  spiral phase will remain robust under this anisotropy; we leave the investigation on the effects of bond anisotropy for future work. Nevertheless, it remains true that the NN exchanges on both X and Z bonds are dominated by large ferromagnetic Kitaev exchanges and that the Kitaev spin liquid is robust against bond-anisotropies.[1]

In addition to distortions and bond anisotropies, an accurate description of the electronic structure also requires hopping amplitudes beyond the NN level (see Sec. C in [Supplementary Materials](#) for details). These terms would generate further neighbor exchange interactions in the strong coupling theory. However, these exchanges are no more than 10% of those at the NN level. Since we expect that such small further-neighbor interactions do not change our conclusions, we focused on the NN exchange interactions in our manuscript.

To enhance the Kitaev exchange relative to other interactions and to approach the spin-liquid regime of the Kitaev model, strengthening the oxygen-mediated-type hopping ( $t_2$ ) is a viable option. Increasing the on-site Coulomb interaction can further localize the  $t_{2g}$  orbitals, which reduces the amplitudes for direct hopping channels like  $t_1$  and  $t_3$  while oxygen-mediated hopping channels like  $t_2$  are comparatively less affected. In addition, increasing  $U$  has the effect of driving the system deeper into the Mott insulating regime and reducing the strength of further neighbor interactions. Therefore, a  $4d$  variant of the  $\beta$ LIO may offer the right ingredients to enhance the Kitaev exchange.

Indeed, the isoelectronic, 2D honeycomb  $\alpha$ -Li<sub>2</sub>RhO<sub>3</sub> has been synthesized and argued to be a relativistic Mott insulator driven by electronic correlations and SOC.[35] Furthermore, this material does not magnetically order down to 0.5 K, which is an indication of magnetic frustration.[35] We speculate that the hypothetical 3D polymorph—hyperhoneycomb  $\beta$ -Li<sub>2</sub>RhO<sub>3</sub>—may be a less distorted version of  $\alpha$ -Li<sub>2</sub>RhO<sub>3</sub> that has all the right properties to further approach the Kitaev region, in analogy to  $\beta$ LIO.

*Acknowledgments* – This work was supported by the NSERC of Canada and the center for Quantum Materials at the University of Toronto. Computations were mainly performed on the GPC supercomputer at the SciNet HPC Consortium. SciNet is funded by: the Canada Foundation for Innovation under the auspices of Compute Canada; the Government of Ontario; Ontario Research Fund - Research Excellence; and the University of Toronto. HSK thanks to IBS Center for Correlated Electron System in Seoul National University for additional computational resources.

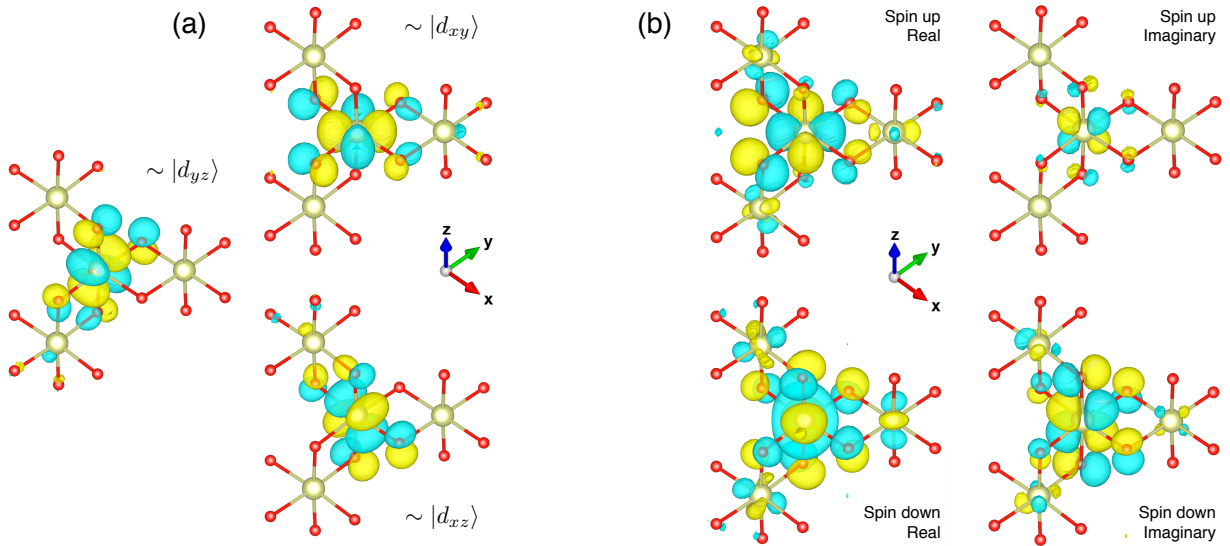


FIG. S1. (Color online) (a) Ir  $t_{2g}$  Wannier orbitals for up spin component located at an Ir site, obtained in a GGA+SOC calculation. Other 21  $t_{2g}$  Wannier orbitals can be obtained by translating them to other Ir sites in the unit cell and applying time-reversal operation. Only nearest-neighboring Ir atoms are shown. (b) One Ir  $j_{\text{eff}}=1/2$  Wannier orbital obtained in a PBE+SO+ $U$  calculation with  $U_{\text{eff}} = 3$  eV. Other eight  $j_{\text{eff}}=1/2$  Wannier orbitals can be obtained by translations and time-reversal operation. Note that, isosurface value for drawing the  $t_{2g}$  Wannier orbital in (a) is twice larger than the one used in (b).

### Details on *ab-initio* electronic structure calculations

For the electronic structure calculations with SOC and on-site Coulomb interaction, OPENMX code[36], which is based on the linear-combination-of-pseudo-atomic-orbital basis formalism, was used. A non-collinear DFT scheme and a fully relativistic  $j$ -dependent pseudopotential were used to treat SOC, and Perdew-Burke-Ernzerhof parametrization of the generalized gradient approximation (GGA) was chosen for the exchange-correlation functional[37], which was compared and found to be almost identical with the results with the Perdew and Zunger local density approximation functional[38]. 400 Ry of energy cutoff was used for the real-space sampling, and  $9 \times 9 \times 9$   $k$ -grid was adopted for the primitive unit cell. Electron interactions are treated as on-site Coulomb interactions via a simplified LDA+ $U$  formalism implemented in OPENMX code[39], and up to 3.0 eV of  $U_{\text{eff}} \equiv U - J_{\text{H}}$  parameter ( $J_{\text{H}}$  is Hund's coupling) was used for Ir  $d$  orbital in our GGA+SOC+ $U$  calculations. Maximally-localized Wannier orbital method[40], which is implemented in OPENMX code[41], were used to obtain the tight-binding Hamiltonian for Ir  $t_{2g}$  atoms.

### Supplementary Material B: Ir $t_{2g}$ and $j_{\text{eff}}=1/2$ Wannier orbitals

In order to obtain the hopping integrals between the Ir  $t_{2g}$  states, the Wannier orbitals for the Ir  $t_{2g}$  bands were calculated in the presence of SOC. Fig. S1 shows the results, where the three  $t_{2g}$  Wannier orbitals at an Ir site with spin up component are shown. Other 21 orbitals at the four Ir sites in the unit cell

are obtained by translating them and applying time-reversal operation  $i\sigma_y\mathcal{K}$ , where  $\sigma_y$  and  $\mathcal{K}$  are the Pauli matrix acting on the spin sector and the complex conjugation, respectively. The oxygen  $p$ -orbital components hybridized into the Ir  $t_{2g}$  bands are manifested as the oxygen  $p$ -orbital tails shown in the figure. Size of oxygen hybridization is slightly enhanced as the value of  $U_{\text{eff}}$  is increased, which contribute to the  $t_2$  hopping term dominated by the oxygen-mediated channel.

The values of the effective SOC strength  $\lambda_{t_{2g}}$  mentioned in the main text were estimated from the on-site energies between the  $t_{2g}$  Wannier orbitals. The on-site energy matrix can be approximately expressed as  $H_{\text{on}} \approx \lambda_{t_{2g}} \mathbf{l}_{t_{2g}} \cdot \mathbf{s} + \Delta_t$ , where  $\Delta_t$  is the minor trigonal crystal field terms. The value of  $\lambda_{t_{2g}}$  for each  $U_{\text{eff}}$  value was obtained by taking the average of the matrix elements corresponding to the SOC term, with their standard deviation smaller than 10% of their average.

Fig. S1(b) shows the  $j_{\text{eff}}=1/2$ -like Wannier orbital, obtained from the low-energy window dominated by the  $j_{\text{eff}}=1/2$  character as illustrated in Fig. 3(c) in the main text, in a GGA+SOC+ $U$  calculation with  $U_{\text{eff}} = 3$  eV. Like the  $t_{2g}$  orbitals, other seven  $j_{\text{eff}}=1/2$ -like Wannier orbitals in the unit cell can be obtained by translation and time reversal operations. Decomposing the Wannier orbital in terms of the local Ir  $t_{2g}$  basis reveals the dominant  $j_{\text{eff}}=1/2$  character at the center with the  $j_{\text{eff}}=3/2$ -dominated tails on the three next-neighboring Ir sites, as schematically shown in Fig. 3(c) in the main text. The tail components are gradually reduced as the  $U_{\text{eff}}$  value is increased, so that the Wannier orbital becomes more localized in the presence of higher  $U_{\text{eff}}$ .

### Supplementary Material C:

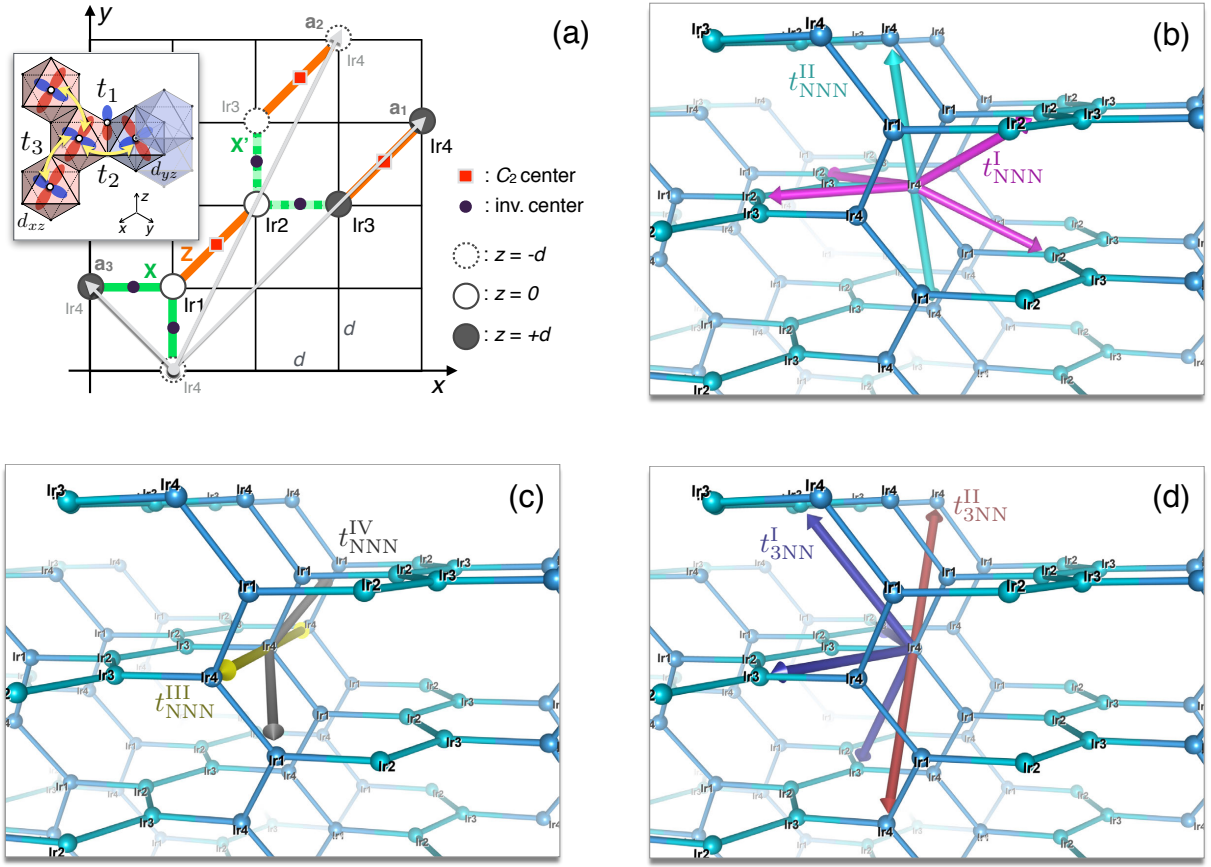


FIG. S2. (Color online) (a) Ir sites projected onto  $xy$ -plane defined in terms of local cubic axes.  $\mathbf{a}_1$ ,  $\mathbf{a}_2$  and  $\mathbf{a}_3$  are the Bravais lattice vector for the primitive cell, where four sublattices within the primitive cell are labeled as Ir1 to Ir4. Centers for  $C_2^{a,b,z}$  rotations and inversion are depicted as red square and black dots on the Z and X ( $X'$ ) bonds, respectively. Note that  $d$  becomes same with the Ir-O bond length in the absence of trigonal distortion. Inset shows the three major hopping channels between NN Ir sites. (b,c) All NNN and (d) third NN neighbors for an Ir site, Ir4, are depicted as colored arrows. Note that different colors (blue and green) are used to distinguish Ir sites and bonds belonging to one zigzag chain to another. (a) shows NNN hopping paths that can be reached through intermediate NN Ir sites. Intra- and inter-chain bonds are colored as cyan and purple, respectively. (b) shows NNN paths that cannot be reached through one NN bonds. Yellow and grey arrows represent paths connecting same (Ir4 to Ir4) and different sublattices (Ir4 to Ir1 in the figure), respectively. (c) shows all third NN hopping paths. Purple and red arrows show bonds connecting different and same sublattices, respectively. Note that, bonds in (b) and red bonds in (c) does not have any counterparts in the 2D honeycomb lattice.

### $t_{2g}$ hopping terms and tight-binding bands from Wannier orbitals

Table S3 shows a partial list of Ir  $t_{2g}$  hopping terms (up to third NN) from the Wannier orbitals, where the convention for the coordinate system and the illustration of NNN and third NN hopping terms are in Fig. S2. Full list of hopping terms can be restored by applying the  $C_2$  rotations and inversion operations at the centers of Z and X ( $X'$ ) bonds, respectively. Three  $C_2$  rotations —  $C_2^{a,b,z}$  — are allowed, where  $\mathbf{a} \equiv \hat{x} + \hat{y}$  and  $\mathbf{b} \equiv \hat{y} - \hat{x}$ .

Contrary to the relatively simple NN hopping channels as shown in the inset of Fig. S2(a), a number of distinct NNN hopping terms are introduced due to the three-dimensional twisting of the honeycomb lattice[42]. The NNN hopping channels can be classified into two kinds, depending on

whether they are analogous to the NNN hopping in the 2D honeycomb lattice or not. Fig. S2(b) shows the 2D-like NNN hopping channels, which can be reached through one intermediate NN Ir site. Depending on whether they belong to same zigzag chain composed of only X (or  $X'$ ) bonds or connect different chains, they are divided into two different classes  $t_{\text{NNN}}^{\text{I}}$  and  $t_{\text{NNN}}^{\text{II}}$ . Hopping amplitudes in these channels are larger than the other channels,  $t_{\text{NNN}}^{\text{III}}$  and  $t_{\text{NNN}}^{\text{IV}}$ , which cannot be reached through one Ir site as shown in Fig. S2(c). There are also non-negligible third NN hopping terms,  $t_{\text{3NN}}^{\text{I}}$  and  $t_{\text{3NN}}^{\text{II}}$ , which can be seen in Fig. S2(d) and Table S3. Like NNN hopping channels, third NN channels can be classified depending on whether they have their 2D counterparts or not.  $t_{\text{3NN}}^{\text{I}}$  resembles the third NN hopping channel in the 2D honeycomb lattice, while  $t_{\text{3NN}}^{\text{II}}$  is similar to the interlayer hopping terms in  $\alpha$ -AIO series.

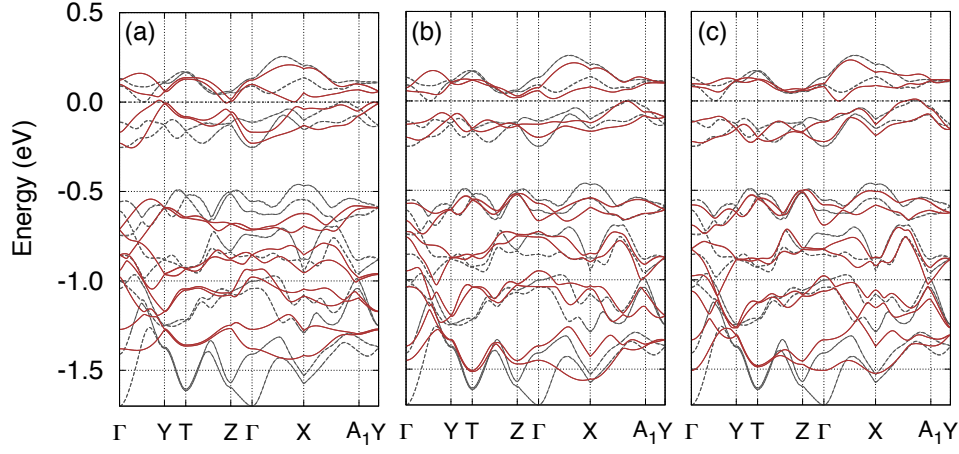


FIG. S3. (Color online) Band structures (solid red lines) calculated from tight-binding calculations including up to (a) NN, (b) NNN, and (c) third-NN hopping terms from the Wannier orbital calculations tabulated in Table. S3, compared to those from *ab-initio* results (dashed grey lines). SOC is included in the calculations.

The role of further-neighbor hopping amplitudes in the band structure are shown in Fig. S3, where the evolution of band structure as we include NNN and third NN terms are presented. Fig. S3 shows the change of the band structures as further-neighbor hopping terms are included with the presence of SOC; Fig. S3(a), (b) and (c) show the bands with hopping terms up to NN, NNN, and third NN terms, respectively, with the presence of SOC. One can see that, the large SOC in Ir tends to make the  $j_{\text{eff}} = 1/2$  bands to be flatter in this locally honeycomb-like lattice, and including NNN and third NN terms does not change the overall behavior. Comparing Fig. S3(a) and Fig. S3(b), one can notice that the dispersion inside the  $j_{\text{eff}} = 1/2$  subbands is affected by the NNN terms, but the semi-metallic character is left unchanged. Inclusion of third NN terms, as can be seen in Fig. S3(c), makes the dispersion slightly closer to the *ab-initio* bands.

#### Supplementary Material D:

TABLE S3: A subset of Ir  $t_{2g}$  hopping terms  $\mathbf{T}_{ij}$  as representatives of each hopping channels up to third NN, where  $\mathcal{H}_{\text{hop}} = \sum_{ij} \mathbf{C}_i^\dagger \cdot \mathbf{T}_{ij} \cdot \mathbf{C}_j$  and  $\mathbf{C}^\dagger$  and  $\mathbf{C}$  being the creation and annihilation operator for  $t_{2g}$  states, respectively.  $d$  is approximate distance between Ir and O. Other hopping terms can be recovered by applying  $\mathbf{T}_{ji} = \mathbf{T}_{ij}^\dagger$ ,  $C_2^{a,b,z}$  rotations, and inversion operations.

Kind	$\mathbf{r}_{ij}$ (in Cartesian coord.)	Sublattice	$U_{\text{eff}} = 0.0 \text{ eV}$			$U_{\text{eff}} = 1.5 \text{ eV}$			$U_{\text{eff}} = 3.0 \text{ eV}$			
$t_{\text{NN}}$			$d_{xy}$	$d_{xz}$	$d_{yz}$	$d_{xy}$	$d_{xz}$	$d_{yz}$	$d_{xy}$	$d_{xz}$	$d_{yz}$	
X,X'	$(-d, 0, +d)$	$1 \rightarrow 4$	$d_{xy}$	+0.088	+0.018	+0.260	+0.080	+0.019	+0.276	+0.064	+0.021	+0.289
			$d_{xz}$	+0.018	-0.152	+0.013	+0.020	-0.110	+0.013	+0.021	-0.051	0.005
			$d_{yz}$	+0.259	+0.013	+0.078	+0.276	+0.013	+0.067	+0.288	0.003	+0.052
$t_{\text{NN}}$			$d_{xy}$	$d_{xz}$	$d_{yz}$	$d_{xy}$	$d_{xz}$	$d_{yz}$	$d_{xy}$	$d_{xz}$	$d_{yz}$	
Z	$(+d, +d, 0)$	$1 \rightarrow 2$	$d_{xy}$	-0.162	-0.022	+0.021	-0.119	-0.024	+0.023	-0.059	-0.031	+0.030
			$d_{xz}$	+0.016	+0.087	-0.239	+0.017	+0.078	-0.255	+0.025	+0.072	-0.269
			$d_{yz}$	-0.016	-0.239	+0.086	-0.017	-0.254	+0.077	-0.024	-0.271	+0.056

Continued in next page...

#### NN exchange interactions

The exchanges  $J$ ,  $K$ , and  $\Gamma$  are given by (suppressing the bond label  $\alpha$ )

$$J = \frac{4}{27} \left[ \frac{(2t_1 + t_3)^2 (4J_H + 3U)}{U^2} - \frac{16J_H(t_1 - t_3)^2}{(2U + 3\lambda)^2} \right]$$

$$K = \frac{32J_H}{9} \left[ \frac{(t_1 - t_3)^2 - 3t_2^2}{(2U + 3\lambda)^2} \right], \Gamma = \frac{64J_H}{9} \frac{t_2(t_1 - t_3)}{(2U + 3\lambda)^2}, \quad (1)$$

where  $t_i$  ( $i = 1, 2, 3$ ),  $J_H$ ,  $U$ , and  $\lambda$  are the NN hopping amplitudes, Hund's coupling, on-site Coulomb repulsion, and SOC respectively[9].  $t_i$  is illustrated in Fig. S2(a). Note that, the small amount of NN Heisenberg interaction is attributed to the cancelation between the  $2t_1$  and  $t_3$  in the antiferromagnetic contribution to  $J$  in Eq. 1. Since  $t_2$  is the largest term, as mentioned in the main text, ferromagnetic  $K$  becomes the most dominant contribution in the exchange interactions.

Continued from previous page...

Kind	$r_{ij}$ (in Cartesian coord.)	Sublattice	$U_{\text{eff}} = 0.0 \text{ eV}$			$U_{\text{eff}} = 1.5 \text{ eV}$			$U_{\text{eff}} = 3.0 \text{ eV}$			
			$d_{xy}$	$d_{xz}$	$d_{yz}$	$d_{xy}$	$d_{xz}$	$d_{yz}$	$d_{xy}$	$d_{xz}$	$d_{yz}$	
$t_{\text{NNN}}^{\text{I}}$	$(+d,+2d,-d)$	1 $\rightarrow$ 3	$d_{xy}$	0.002	-0.012	+0.039	0.001	-0.015	+0.044	0.001	-0.018	+0.047
			$d_{xz}$	+0.013	0.001	+0.011	+0.018	0.001	+0.014	+0.024	0.001	+0.017
			$d_{yz}$	+0.063	0.004	0.002	+0.075	0.007	0.000	+0.089	-0.010	0.001
$t_{\text{NNN}}^{\text{II}}$	$(-d,+d,+2d)$	1 $\rightarrow$ 1	$d_{xy}$	0.002	0.008	-0.014	0.003	-0.011	-0.017	0.003	-0.014	-0.020
			$d_{xz}$	+0.014	0.001	+0.039	+0.017	0.000	+0.045	+0.020	0.002	+0.050
			$d_{yz}$	0.008	+0.075	0.001	+0.011	+0.089	0.000	+0.014	+0.103	0.001
$t_{\text{NNN}}^{\text{III}}$	$(-d,+d,-2d)$	1 $\rightarrow$ 1	$d_{xy}$	0.001	+0.011	0.001	0.000	+0.013	0.000	0.002	+0.015	0.003
			$d_{xz}$	0.001	0.007	+0.038	0.000	0.005	+0.045	0.003	0.002	+0.051
			$d_{yz}$	-0.011	+0.030	0.008	-0.013	+0.036	0.006	-0.015	+0.047	0.004
$t_{\text{NNN}}^{\text{IV}}$	$(+d,-2d,+d)$	1 $\rightarrow$ 4	$d_{xy}$	+0.012	0.007	-0.030	0.009	0.008	-0.035	0.005	0.008	-0.041
			$d_{xz}$	0.007	0.008	0.006	0.008	0.009	0.008	0.008	+0.011	0.008
			$d_{yz}$	-0.030	0.007	0.003	-0.035	0.008	0.007	-0.041	0.008	-0.012
$t_{\text{3NN}}^{\text{I}}$	$(0,+2d,-2d)$	1 $\rightarrow$ 2	$d_{xy}$	0.007	-0.013	-0.014	0.007	-0.014	-0.015	0.008	-0.015	-0.017
			$d_{xz}$	0.008	0.006	0.006	0.009	0.008	0.007	-0.011	+0.011	0.009
			$d_{yz}$	-0.014	-0.016	-0.034	-0.015	-0.018	-0.030	-0.017	-0.020	-0.022
$t_{\text{3NN}}^{\text{II}}$	$(-d,+d,0)$	1 $\rightarrow$ 1	$d_{xy}$	-0.045	0.006	-0.012	-0.046	0.007	-0.013	-0.046	-0.010	-0.013
			$d_{xz}$	+0.012	0.008	0.001	+0.013	0.009	0.001	+0.013	+0.012	0.002
			$d_{yz}$	0.006	-0.015	0.008	0.008	-0.017	0.009	+0.010	-0.018	+0.012

- [1] A. Kitaev, *Ann. Phys.* **321**, 2 (2006).
- [2] Y. Singh, S. Manni, J. Reuther, T. Berlijn, R. Thomale, W. Ku, S. Trebst, and P. Gegenwart, *Phys. Rev. Lett.* **108**, 127203 (2012).
- [3] S. K. Choi, R. Coldea, A. N. Kolmogorov, T. Lancaster, I. I. Mazin, S. J. Blundell, P. G. Radaelli, Y. Singh, P. Gegenwart, K. R. Choi, S.-W. Cheong, P. J. Baker, C. Stock, and J. Taylor, *Phys. Rev. Lett.* **108**, 127204 (2012).
- [4] F. Ye, S. Chi, H. Cao, B. C. Chakoumakos, J. A. Fernandez-Baca, R. Custelcean, T. F. Qi, O. B. Korneta, and G. Cao, *Phys. Rev. B* **85**, 180403(R) (2012).
- [5] B. Kim, H. Jin, S. Moon, J.-Y. Kim, B.-G. Park, C. Leem, J. Yu, T. Noh, C. Kim, S.-J. Oh, *et al.*, *Phys. Rev. Lett.* **101**, 076402 (2008).
- [6] A. Shitade, H. Katsura, J. Kuneš, X.-L. Qi, S.-C. Zhang, and N. Nagaosa, *Phys. Rev. Lett.* **102**, 256403 (2009).
- [7] H. Gretarsson, J. P. Clancy, X. Liu, J. P. Hill, E. Bozin, Y. Singh, S. Manni, P. Gegenwart, J. Kim, A. H. Said, D. Casa, T. Gog, M. H. Upton, H.-S. Kim, J. Yu, V. M. Katukuri, L. Hozoi, J. van den Brink, and Y.-J. Kim, *Phys. Rev. Lett.* **110**, 076402 (2013).
- [8] G. Jackeli and G. Khaliullin, *Phys. Rev. Lett.* **102**, 017205 (2009).
- [9] J. G. Rau, E. K.-H. Lee, and H.-Y. Kee, *Phys. Rev. Lett.* **112**, 077204 (2014).
- [10] M. J. O'Malley, H. Verweij, and P. M. Woodward, *Journal of Solid State Chemistry* **181**, 1803 (2008).
- [11] E. K.-H. Lee and Y. B. Kim, *Phys. Rev. B* **91**, 064407 (2015).
- [12] A. Biffin, R. D. Johnson, S. Choi, F. Freund, S. Manni, A. Bombardi, P. Manuel, P. Gegenwart, and R. Coldea, *Phys. Rev. B* **90**, 205116 (2014).
- [13] T. Takayama, A. Kato, R. Dinnebier, J. Nuss, H. Kono, L. S. I. Veiga, G. Fabbris, D. Haskel, and H. Takagi, *Phys. Rev. Lett.* **114**, 077202 (2015).
- [14] S. Mandal and N. Surendran, *Phys. Rev. B* **79**, 024426 (2009).
- [15] E. K.-H. Lee, R. Schaffer, S. Bhattacharjee, and Y. B. Kim, *Phys. Rev. B* **89**, 045117 (2014).
- [16] I. Kimchi, J. G. Analytis, and A. Vishwanath, *Phys. Rev. B* **90**, 205126 (2014).
- [17] J. Nasu, T. Kaji, K. Matsuura, M. Udagawa, and Y. Motome, *Phys. Rev. B* **89**, 115125 (2014).
- [18] R. Schaffer, E. K.-H. Lee, Y.-M. Lu, and Y. B. Kim, *Phys. Rev. Lett.* **114**, 116803 (2015).
- [19] G.-Q. Liu, V. N. Antonov, O. Jepsen, and O. K. Andersen, *Phys. Rev. Lett.* **101**, 026408 (2008).
- [20] H.-S. Kim, Y. Chen, and H.-Y. Kee, *Phys. Rev. B* **91**, 235103 (2015).
- [21] H.-S. Kim, V. S. V., A. Catuneanu, and H.-Y. Kee, *Phys. Rev. B* **91**, 241110 (2015).
- [22] K. A. Modic, T. E. Smidt, I. Kimchi, N. P. Breznay, A. Biffin, S. Choi, R. D. Johnson, R. Coldea, P. Watkins-Curry, G. T. McCandless, J. Y. Chan, F. Gandara, Z. Islam, A. Vishwanath, A. Shekhter, R. D. McDonald, and J. G. Analytis, *Nature*



Comm. **5**, 4203 (2014).

- [23] See Sec. A in **Supplementary Materials** posted in the author's personal web page (<https://sites.google.com/site/heungsikim/home/temporary-files>) for details.
- [24] We comment that, due to the loss of chiral symmetry and the mixing of the  $j_{\text{eff}} = 3/2$  states in the  $j_{\text{eff}} = 1/2$  subspace, the nodal Fermi ring mentioned in previous tight-binding analysis is absent in both of the ideal and experimental structures.
- [25] In order to capture the role of electron correlations in the band structure only, we do not consider any magnetism in our DFT+ $U$  calculations in this work.
- [26] See **Supplementary Materials** for further details.
- [27] We note this SOC enhancement in  $\beta\text{LIO}$  is less significant compared to other systems because the  $j_{\text{eff}} = 1/2$  and  $3/2$  states were already well-separated when  $U_{\text{eff}} = 0$  eV as a result of large SOC.
- [28] H.-S. Kim, C. H. Kim, H. Jeong, H. Jin, and J. Yu, **Phys. Rev. B** **87**, 165117 (2013).
- [29] C. H. Sohn, H.-S. Kim, T. F. Qi, D. W. Jeong, H. J. Park, H. K. Yoo, H. H. Kim, J.-Y. Kim, T. D. Kang, D.-Y. Cho, G. Cao, J. Yu, S. J. Moon, and T. W. Noh, **Phys. Rev. B** **88**, 085125 (2013).
- [30] I. I. Mazin, H. O. Jeschke, K. Foyevtsova, R. Valentí, and D. I. Khomskii, **Phys. Rev. Lett.** **109**, 197201 (2012).
- [31] C. H. Kim, H. S. Kim, H. Jeong, H. Jin, and J. Yu, **Phys. Rev. Lett.** **108**, 106401 (2012).
- [32] Such *ab-initio* based perturbative approach applied to  $\text{Na}_2\text{IrO}_3$ [43] yielded consistent results with the state-of-the-art quantum chemistry calculation performed in Ref. [44].
- [33] The ranges of  $U_{\text{eff}}$  and  $J_{\text{H}}$  we used in this work are consistent with recent constrained RPA calculations of both parameters in the Ir  $5d$  orbitals[43, 45].
- [34] For  $U_{\text{eff}}$  and  $J_{\text{H}}$ , we chose the triangular and uniform distributions respectively for the stated ranges. The qualitative features of the resulting exchange parameters' density distribution are not dependent on the precise distribution used but only on the mean and range of the distribution.
- [35] Y. Luo, C. Cao, B. Si, Y. Li, J. Bao, H. Guo, X. Yang, C. Shen, C. Feng, J. Dai, *et al.*, **Phys. Rev. B** **87**, 161121 (2013).
- [36] T. Ozaki, **Phys. Rev. B** **67**, 155108; <http://www.openmx-square.org>.
- [37] J. P. Perdew, K. Burke, and M. Ernzerhof, **Phys. Rev. Lett.** **77**, 3865 (1996).
- [38] D. M. Ceperley and B. J. Alder, **Phys. Rev. Lett.** **45**, 566 (1980); J. P. Perdew and A. Zunger, **Phys. Rev. B** **23**, 5048 (1981).
- [39] M. J. Han, T. Ozaki, and J. Yu, **Phys. Rev. B** **73**, 045110 (2006).
- [40] N. Marzari and D. Vanderbilt, **Phys. Rev. B** **56**, 12847 (1997).
- [41] H. Weng, T. Ozaki, and K. Terakura, **Phys. Rev. B** **79**, 235118 (2009).
- [42] E. K.-H. Lee, S. Bhattacharjee, K. Hwang, H.-S. Kim, H. Jin, and Y. B. Kim, **Phys. Rev. B** **89**, 205132 (2014).
- [43] Y. Yamaji, Y. Nomura, M. Kurita, R. Arita, and M. Imada, **Phys. Rev. Lett.** **113**, 107201 (2014).
- [44] V. M. Katukuri, S. Nishimoto, V. Yushankhai, A. Stoyanova, H. Kandpal, S. Choi, R. Coldea, I. Rousochatzakis, L. Hozoi, and J. van den Brink, **New Journal of Physics** **16**, 013056 (2014).
- [45] E. Şaşıoğlu, C. Friedrich, and S. Blügel, **Phys. Rev. B** **83**, 121101 (2011).